Upstream and Downstream Influence on the Unsteadiness of STBLI using DNS Data

M. Pino MARTIN and Minwei WU

Princeton University, Mechanical and Aerospace Engineering Department, Princeton, NJ 08540, USA,

pmartin@princeton.edu

Abstract. Direct numerical simulation data of a 24° compression ramp configuration are used to analyze the shock motion. The characteristic frequencies in the incoming boundary layer are reported for reference. The shock wave motion exhibits high-frequency spanwise wrinkling, as well as low-frequency streamwise motion. Correlations between the incoming flow and the shock motions, as well as the downstream flow and the shock unsteadiness are investigated. In addition, analyses show that the unsteadiness of the separation bubble correlates with low-frequency shock motion, giving a Strouhal number of 0.8 based on the low-frequency of the shock motion, the length of the separation bubble and the averaged maximum velocity of reversed flow.

Key words: turbulence, shock wave, boundary layer, DNS, compressible flow.

1. Introduction

One of the key features of shockwave and turbulent boundary layer interactions (STBLI) is the unsteady motion of the shock [2, 5, 6, 7, 12, 19, 20, 21, 22]. For two-dimensional interactions, such as those produced by a compression ramp, the shock moves back and forth in the streamwise direction and displays significant transverse distortions [9, 24, 25]. The typical frequency of shock unsteadiness is one to two orders of magnitude lower than that characteristic of the undisturbed incoming boundary layer, U_e /δ. The streamwise extent of the shock movement increases with shock strength. The mechanism driving the shock motion is still a subject of debate. Plotkin [15] proposed a damped spring model for the shock motion. Andreopoulos & Muck [1] concluded that the shock motion is driven by the bursting events in the incoming boundary layer. However, Thomas et al. [23] found no connection between the shock motion and bursting events in the incoming boundary layer. Erengil & Dolling [8] found that there was a correlation between certain shock motions with pressure fluctuations in the incoming boundary layer. Beresh et al. [3] found that positive velocity fluctuations near the wall correlate with downstream shock motion. Pirozzoli & Grasso [14] analyzed DNS data of a reflected shock interaction and proposed that a resonance mechanism might be responsible for the shock unsteadiness. Dussauge et al. [7] suggested that the three-dimensional nature of the interaction in the reflected shock configuration is a key to understanding the shock unsteadiness. Ganapathisubramani et al. [9] proposed that very long alternating

structures of uniform low- and high-speed fluid in the logarithmic region of the incoming boundary layer are responsible for the low frequency motion of the shock. These so called 'superstructures' have been observed in supersonic boundary layers by Samimy et al. [18] and are also evident in the elongated wall-pressure correlation measurements of Owen & Horstmann [13]. Superstructures have also been observed in the atmospheric boundary layer experiments of Hutchins & Marusic [11] and confirmed in DNS of supersonic boundary layers by Ringuette et al. [17].

In this paper, we analyze DNS data to study the effect of the incoming boundary layer on the shock motion. In addition, we study the correlation between the downstream flow and the shock motion, as well as the characteristics of the separation bubble unsteadiness. In Section 2, we summarize the flow configuration and conditions, as well as details of the DNS data. In Section 3, we describe relevant features of the incoming boundary layer. In Section 4, we illustrate the characteristics of the shock unsteadiness. In Section 5, we present the correlation between the upstream flow and downstream flow with the shock motions. In Section 6, we characterize the separation bubble unsteadiness and its correlation with the shock motion. In Section 7, we present the conclusions from the analyses.

2. Direct Numerical Simulation Data

We use the DNS data of STBLI for a 24° compression ramp configuration at Mach 2.9 and Reynolds number based on momentum thickness of 2300 from Wu & Martin [24]. Table 1 lists the inflow boundary layer conditions. Figure 1 shows the computational domain and the coordinate system for the STBLI. Notice that we use z_n to denote the wall-normal coordinate. The boundary conditions are periodic in the spanwise direction and the inflow condition is provided using a recycling technique [26]. The recycling location is 4.5δ downstream of the inlet, as shown in Figure 1. Prime symbols are used to denote fluctuating quantities. Statistics are gathered over $300\delta/U_\infty$.

Wu & Martin [24] validate the data against the experiments of Bookey et al. [4] at matching flow conditions. They show the agreement in the mean wall-pressure distribution, mean velocity profiles upstream and downstream of the interaction, and the separation size. Figure 2a plots the mean wall-pressure distribution for the DNS and experimental data. The compression corner is centered at x=0. The error bars indicate a 5% uncertainty in the measurement and the DNS predicts the experiments within the experimental uncertainty. Figure 2b plots the magnitude of wall pressure fluctuations for the DNS and experiments [16]. The DNS slightly over-predict the level of fluctuations in the incoming boundary layer due to the synthetically prescribed structures in the initial condition. Experimental data are very recent, and uncertainty analyses

Table 1. Inflow conditions for the DNS. The Mach number, Reynolds number based on the momentum thickness, displacement thickness, boundary layer thickness, boundary layer thickness in wall variables, and skin friction are given in order of appearance.

M	Re_θ	θ (mm)	δ^* (mm)	δ (mm)	δ^+	C_f
2.9	2300	0.38	1.80	6.4	320	0.0021

have not been performed yet. The trend and the peak of fluctuations show good agreement.

3. Turbulence Structure in the Incoming Boundary Layer

The use of a recycling inflow boundary condition results in a forcing frequency of $0.22U_\infty / \delta$. Figure 3 plots contours of $|\nabla\rho|$ up-stream of the compression corner, showing the characteristic recycled structure. Figure 4a plots the frequency content of the normalized (by the average) mass-flux signals for x=-6.9δ and various wall-normal locations. For both signals, the forcing can be observed at $f = 0.22U_\infty / \delta$. Figure 4b plots the premultiplied frequency spectrum for the wall-pressure signals at the same streamwise location, showing that there is no forcing at the wall due to the recycling boundary condition. Instead, the dominant frequency is at $0.6U_\infty / \delta$. Figure 5 plots a rake signal of streamwise velocity at z_n=0.2δ, with the *x*-axis reconstructed using Taylor's hypothesis with $0.76U_\infty$. The superstructures, i.e. long regions of uniformly low velocity [10, 11] can be observed. It is useful noticing that no effect of the recycling condition is observed as no structures extend the entire domain, instead structures end and begin within the domain a various locations, some of which are highlighted within circles in Figure 5.

4. Characteristics of the Unsteady Shock Wave

Figure 6 plots contours of the magnitude of the pressure gradient on streamwise-spanwise planes. Two instantaneous flow fields are plotted at z_n=0.9δ and 2δ. At z_n=2δ in Figures 6 (a) and (b), the shock is nearly uniform in the spanwise direction. The streamwise movement of the shock is roughly 1δ. Figures 6 (c) and (d) plot two planes closer to the wall for the same temporal realizations. We observe a wrinkling of the shock in the spanwise direction, with amplitude of about 0.5δ. At z_n=0.9δ, the shock also moves in the streamwise direction in the

same manner as in the free stream, by about 1δ. The amplitude of the motion in the streamwise direction is twice that of the spanwise wrinkling.

Figure 7 plots the pre-multiplied energy spectrum for wall-pressure signals at the separation point $x=-2.98\delta$ and inside of the separation bubble $x=-2.18\delta$. Two dominant frequencies are observed, $f_{high}=0.6U_\infty/\delta$ and f_{low} in $0.007U_\infty/\delta$ to $0.01U_\infty/\delta$.

5. Upstream and Downstream Influence

To study the effect of the upstream and downstream flow on the shock unsteadiness, we consider the co-spectrum of the mass-flux signal in the boundary layer and the pressure signal at the mean shock location. In high Reynolds number flows, the shock location is inferred from wall-pressure measurements. In contrast at low Reynolds numbers, such as that considered here, the viscous effects are more prominent, the shock does not penetrate as deeply as in higher Reynolds number flows, and the shock location is not well defined in the lower half of the boundary layer. A comparison between high and low Reynolds number data of STBLI has been recently presented by Ringuette, and Smits [16]. For this reason we perform the co-spectrum analysis for signals that are measured at $z_n=0.7\delta$. Figure 8a shows the location were the signals are measured. Figure 8b plots the corresponding co-spectrum showing that the upstream flow and the shock motion are most correlated at a high frequency, which corresponds to the recycling frequency. Figure 9 plots iso-surfaces of the gradient of density at two instantaneous realizations that are $1\delta/U_\infty$ apart in time. A large eddy structure is identified with an arrow and seen to convect through the shock at the second frame. As the low-velocity, low-density fluid convects through the shock, the shock relaxes upstream. Figures 8 and 9 show that the high-frequency shock motion is a result of eddies convecting through the shock, causing the shock to wrinkle in the spanwise direction.

Figure 10 shows the corresponding data for the co-spectrum between the pressure at the mean shock location and the mass flux downstream at reattachment and downstream of the interaction region. For the signals downstream of the interaction, characteristic low frequencies of about $0.007\delta/U_\infty$ to $0.013\delta/U_\infty$ and high frequency of about $0.22\delta/U_\infty$ are dominant. The high-frequency corresponds with that of the recycled structures. For the data at the reattachment point, the low frequency is not dominant. It is believed that the dynamics of the interaction at the reattachment point are confined to the wall region and at $z_n=0.7\delta$, the low frequency characteristics are not apparent. Figure 10 shows that the low-frequency shock motion is affected by the dynamics of the downstream flow.

6. Unsteadiness of the Separation Bubble and Correlation with Shock Motion

Dussauge, Dupont and Debiève [7] define a Strouhal number based on the separation length and the free stream velocity, $St_L = fL_{sep}/U_\infty$. They find that experimental data covering a range of Mach numbers, Reynolds numbers and various configurations, the data are grouped in St_L = 0.02 and 0.05. For the present DNS data, St_L =0.03-0.042. Replacing the free stream velocity with the average maximum reversed flow gives $St_{LUr} = 0.8$. It is useful noticing that if we believe the scaling proposed by Dussauge et al, the separation length can be inferred from the empirical relation described in Zheltovodov et al. [27] with the plateau pressure given in the empirical formula of Zukoski [28] to obtain a frequency range.

Figure 11 plots the temporal evolution of the spanwise averaged separation and reattachment points, defined using a zero-skin-friction criteria. The separation and reattachment move towards and away from each other with a characteristic low frequency. Figure 12 plots the temporal evolution of the mass and volume of the reversed flow in the separation bubble. The density remains constant in time and the bubble shrinks and grows due to the fluid leaving and entering the region. Figure 13 plots the coherency functions for the shock location with the separation and reattachment points, the signals are highly correlated in the low frequency range. Figure 14 plots the correlation between the separation and reattachment points and the correlation between the shock location and the reattachment point. Both correlations are negative, showing that the separation point and the shock move in the opposite direction to that of the reattachment point. In addition, the time lags are negative, showing that the motion of the shock and the reattachment point lag that of the reattachment point. This indicates that the motion of the shock is driven by the fluid in the separation regions, downstream of the shock.

7. Conclusions

Analyses of the direct numerical simulation data for turbulent Mach 2.9 flow over a 24° compression ramp indicate that the shock unsteadiness is characterized by low- and high-frequency motions. The mass flux in the incoming boundary layer is correlated with the high-frequency spanwise wrinkling motion, as turbulent eddies convect through the shock and cause the high-frequency $\vartheta(U_\infty/\delta)$ motion. The low-frequency motion is caused by the unsteadiness of the separation bubble, as the bubble shrinks and grows and the characteristic frequency is about $0.013U_\infty/\delta$ or a Strouhal number of $St_{LUr} = 0.8$. The motions of the shock and the separation point lag that of the reattachment point, indicating that the downstream flow plays an important role in driving the shock unsteadiness.

Acknowledgements

References

1. Andreopoulos, J. and Muck, K.C., Some new aspects of the shock-wave/boundary layer interaction in compression-ramp flows. *J. Fluid Mech.* **180** (July) (1987) 405—428.
2. Ardonceau, P.L., The structure of turbulence in a supersonic shock-wave/boundary layer. *AIAA J.* **22** (9) (1983) 1254—1262.
3. Beresh, S.J., Clemens, N.T. and Dolling, D.S., Relationship between upstream turbulent boundary-layer velocity fluctuations and separation shock unsteadiness. *AIAA J.* **40** (12) (2002) 2412—2423.
4. Bookey, P.B., Wyckham, C., Smits, A.J. and Martin, M.P., New experimental data of STBLI at DNS/LES accessible Reynolds Numbers. *AIAA Paper No. 2005-309* (2005).
5. Dolling, D.S. and Or, C.T., Unsteadiness of the shock wave structure in attached and separated compression ramp flows. *Exp. Fluids* **3** (1) (1985) 24—32.
6. Dupont, P., Haddad, C. and Debiève, J.F., Space and Time Organization in a shock-induced separated boundary layer. *J. Fluid Mech.* **559** (Jul) (2006) 255—277.
7. Dussauge, J.P., Dupont, P. and Debiève, J.F., Unsteadiness in shock wave boundary layer interactions with separation. *Aerosp. Sci. Tech.* **10** (2) (2006) 85—91.
8. Erengil, M.E. and Dolling, D.S., Correlation of separation shock motion with pressure fluctuations in the incoming boundary layer. *AIAA J.* **29** (11) (1991) 1868—1877.
9. Ganapathisubramani, B., Clemens, N.T. and Dolling, D.S., Planar imaging measurements to study the effect of spanwise structure of upstream turbulent boundary layer on shock induced separation. *AIAA Paper No. 2006-324* (2006).
10. Ganapathisubramani, B., Clemens, N.T. and Dolling, D.S., Effects of upstream coherent structures on low-frequency motion of shock-induced turbulent separation. *AIAA Paper No. 2007-1141* (2007).
11. Hutchins, N. and Marusic, I., Evidence of very long meandering features in the logarithmic region of turbulent boundary layers. *J. Fluid Mech.* (in press 2007).
12. Kuntz, D.W., Amatucci, V.A. and Addy, A.L., Turbulent boundary-layer properties downstream of the shock-wave/boundary-layer interaction. *AIAA J.* **25** (1987) 668—675.
13. Owen, F. and Horstmann, C., On the structure of hypersonic turbulent boundary layers. *J. Fluid Mech.* **53** (1972) 611—636.
14. Pirozzoli, S. and Grasso, F., Direct numerical simulation of impinging shock wave/turbulent boundary layer interaction at $M = 2.25$. *Phys. Fluids* **18** (6) (2006).
15. Plotkin, K., Shock wave oscillation driven by turbulent boundary-layer fluctuations. *AIAA J.* **13** (8) (1975) 1036—1040.
16. Ringuette, M.J. and Smits, A.J., Wall-pressure measurements in a Mach 3 shock-wave turbulent boundary layer interaction at a DNS-accessible Reynolds Number. *AIAA Paper No. 2007-4113* (2007).
17. Ringuette, M.J., Wu, M. and Martin, M.P., Coherent structures in DNS of supersonic turbulent boundary layers at Mach 3. Under consideration in *J. Fluid Mech.* (2007). Also, *AIAA Paper No. 2007-1138* (2007).

18. Samimy, M., Arnette, S.A. and Elliott, G.S., Streamwise Structures in a Turbulent Supersonic Boundary Layer. *Phys. Fluids* **6** (3) (1994) 1081—1083.
19. Selig, M.S., Unsteadiness of shock wave/turbulent boundary layer interactions with dynamic control. *Ph.D. thesis*, Princeton University (1988).
20. Settles, G.S., Fitzpatrick, T. and Bogdonoff, S.M., Detailed study of attached and separated compression corner flowfields in high Reynolds Number supersonic flow. *AIAA J.* **17** (6) (1979) 579—585.
21. Smith, D.R., Poggie, J., Konrad, W. and Smits, A.J., Visualization of the structure of shock wave turbulent boundary layer interactions using Rayleigh Scattering. *AIAA Paper No. 91-0651* (1991).
22. Smits, A.J. and Muck, K.C., Experimental study of three shock wave/turbulent boundary layer interactions. *J. Fluid Mech.* **182** (Sep) (1987) 291—314.
23. Thomas, F.O., Putnam, C.M. and Chu, H., On the mechanism of unsteady shock oscillation in shock wave/turbulent boundary layer interactions. *Exp. Fluids* **18** (1994) 69—81.
24. Wu, M. and Martin, M.P., Direct numerical simulation of shockwave and turbulent boundary layer interaction induced by a compression ramp. *AIAA J.* **45** (4) (2007) 879—889.
25. Wu, P., Lempert, W.R. and Miles, R.B., Megahertz pulse-burst laser and visualization of shock-wave/boundary-layer interaction. *AIAA J.* **38** (4) (2000) 672—679.
26. Xu, S. and Martin, M.P., Assessment of inflow boundary conditions for compressible turbulent boundary layers. *Phys. Fluids* **16** (7) (2004) 2623—2639.
27. Zheltovodov, A.A., Schülein, E. and Horstman, C., Development of separation in the region where a shock interacts with a turbulent boundary layer perturbed by rarefaction waves. *J. Appl. Mech. Tech. Phys.* **34** (3) (1993) 346—354.
28. Zukoski, E., Turbulent boundary layer separation in front of a forward facing step. *AIAA J.* **5** (10) (1967) 1746—1753.
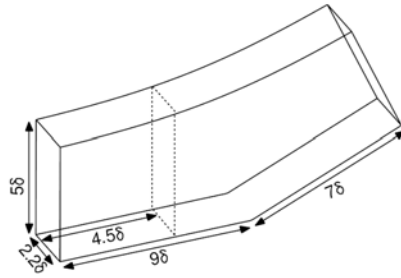
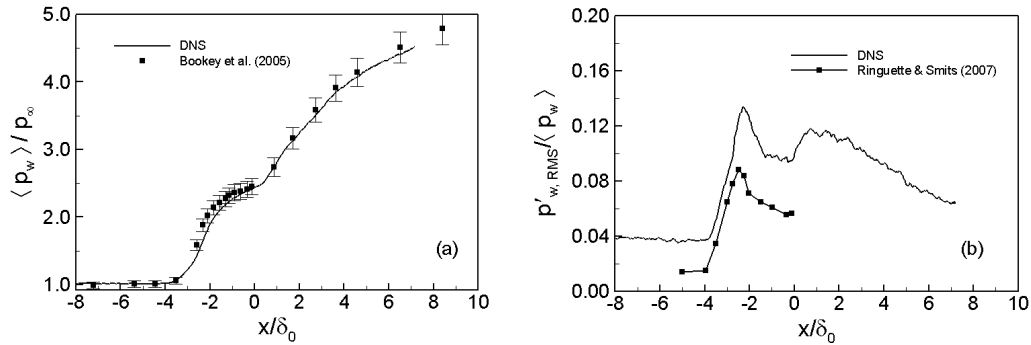*Figure 1*. Computational domain and recycling station for the DNS.

Figure 2. (a) Mean wall-pressure distribution and (b) magnitude of wall-pressure fluctuations for DNS (Wu & Martin 2007) and experimental data at the same conditions: Bookey et al. (2005) with error bars at 5%; Ringuette & Smits (2007).
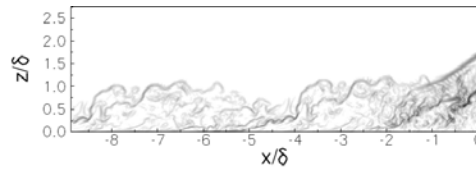

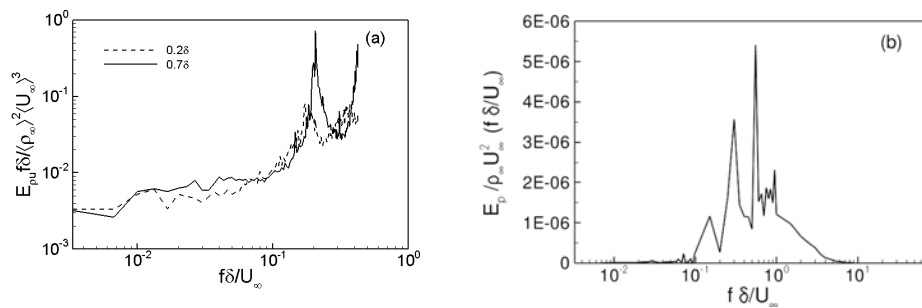*Figure 3*. Instantaneous contours of $|\nabla\rho|$ from DNS data at $y = 1.1\delta$.

Figure 4. Premultiplied energy spectra for the incoming boundary layer. (a) u at two wall-normal locations and $x = -6.9\delta$ and (b) wall-pressure at $x = -6.9\delta$.
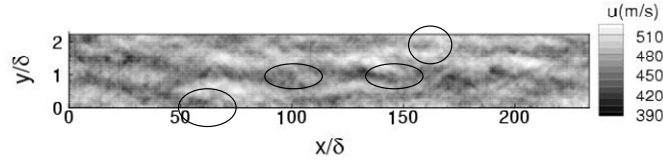
Figure 5. Rake signal of streamwise velocity from DNS data at $z_n = 0.2\delta$. The x axis is reconstructed using Taylor's hypothesis and a convection velocity of $0.76U_\infty$. Data are averaged along the streamwise direction in 4δ from Wu & Martin (2007).
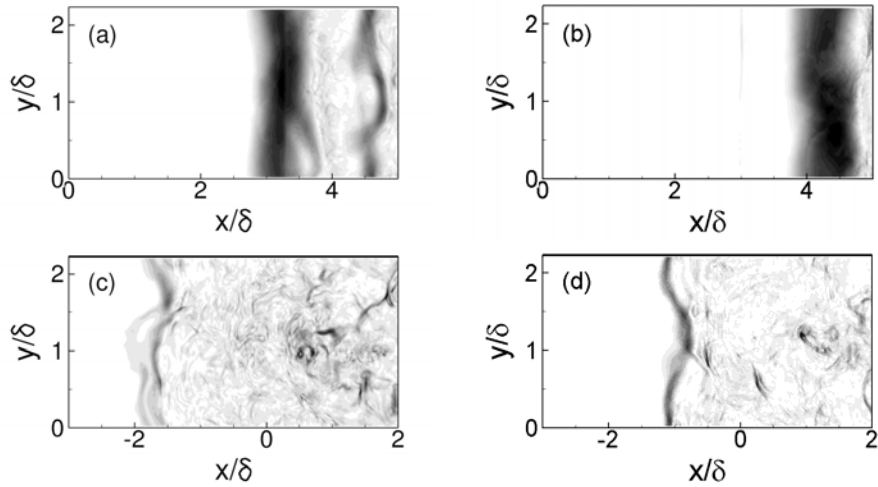
Figure 6. Contours of $|\nabla p|$ showing the shock location for two flow realizations separated by $50\,\delta\,/\,U_\infty$ at $z_n = 2\delta$ ((a) and (b)) and $z_n = 0.9\delta$ ((c) and (d)).
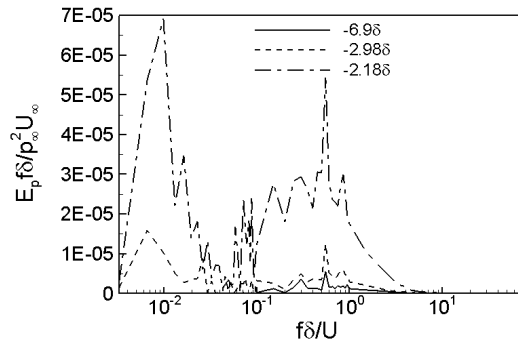
Figure 7. Pre-multiplied energy spectra for wall-pressure signals for at the incoming boundary layer, mean separation point and inside the separated region with $y = 1.1\delta$.
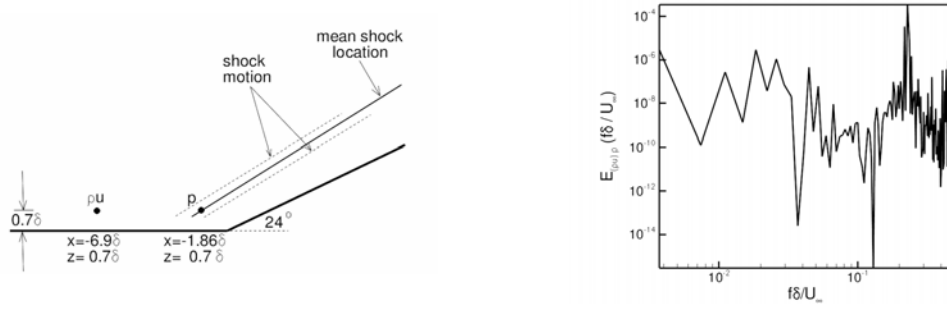
Figure 8. Spanwise averaged, pre-multiplied co-spectrum between the mass-flux in the incoming boundary layer at ($x = -6\delta, y, z_n = 0.7\delta$) and the pressure at the mean shock location ($x_{shock}, y, z_n = 0.7\delta$). (a) Sketch showing the point measurements, (b) data.
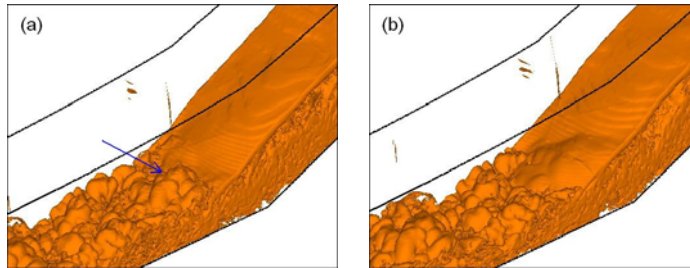

Figure 9. Iso-surface of $\nabla\rho = 2\rho_\infty / \delta$ showing structures in the incoming boundary layer passing through the shock. Temporal spacing between each frame is δ / U_∞.
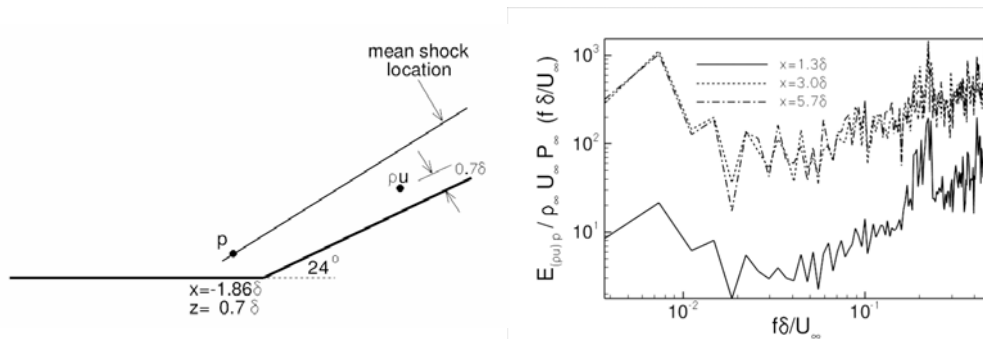

Figure 10. Spanwise averaged, pre-multiplied co-spectrum between the mass-flux in the boundary layer downstream of the interaction at reattachment ($x=1.3\delta$) and two other locations downstream of the reattachment point with ($z_n = 0.7\delta$) and the pressure at the mean shock location ($x_{shock}, y, z_n = 0.7\delta$). (a) Sketch showing the point measurements, (b) data.
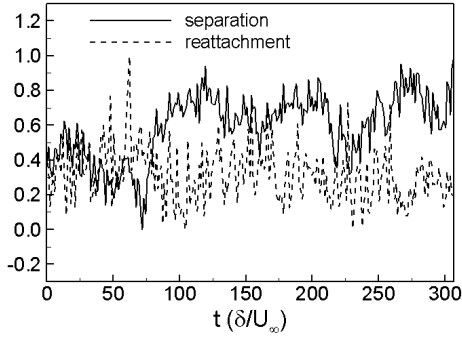
Figure 11. Temporal evolution of the spanwise mean separation (solid) and reattachment (dashed) points.
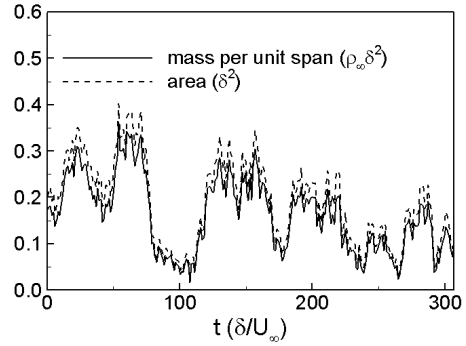

Figure 12. Temporal evolution of various quantities: (solid) "bubble" mass and (dashed) "bubble" volume.
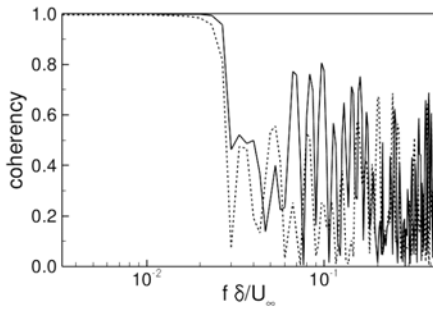

Figure 13. Coherency function between the spanwise-mean shock location at $z_n = 2\delta$ and the (solid) spanwise-mean separation point and (dashed) spanwise-mean reattachment point.
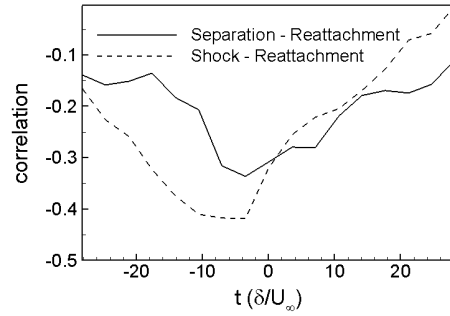

Figure 14. Correlations with time lag: (solid) separation and reattachment points, (dashed) separation point and shock location at $z_n = 2$, (dashed-dotted) reattachment point and shock location at. All locations are spanwise-mean values.